Special Feature: Analysis Techniques to Evaluate the Next Generation Electronic Materials

Research Report

2D Crystal Structure Determination of Bilayer Silicene and Germanene Using Transmission Electron Microscopy

Tetsu Ohsuna, Ritsuko Yaokawa and Hideyuki Nakano

Report received on Jan. 30, 2019

ABSTRACT Two new 2D crystals of bilayer silicene and germanene were recently identified in the fluorinated Zintl phase crystallites of $CaSi_2$ and $CaGe_2$, respectively.[1,2] These crystals have the same atomic structure, which consists of 4-, 5-, and 6-membered rings of Si or Ge atoms that form a wavy shape, and are denoted w-BLSi and w-BLGe, respectively. The crystal structure of w-BLSi had been solved only by atomic resolution electron microscopy with deep insights on the crystallography, because the w-BLSi crystals exist as thin layers in multi-phase layered crystallites and thus X-ray diffraction methods could not be applied. Vacancies of F atoms in the interface plane of neighboring CaF_2 layers were revealed from the contrast in high-angle annular dark-field scanning transmission electron microscopy (HAADF-STEM) images by comparison with simulated images. In this review, we demonstrate the specifications that materials scientists must follow for the structural determination of 2D crystals by the trial and error method.

KEYWORDS Bilayer, Silicene, Germanene, HAADF-STEM, $CaSi_2$, $CaGe_2$, 2D Crystal, w-BLSi, w-BLGe

1. Introduction

Since the discovery of graphene, research on two-dimensional (2D) nanomaterials has rapidly increased due to their extraordinary physical properties.[3-6] There have been many recent theoretical and experimental studies on the atomic layers of heavy group-IV elements (Si: silicene, Ge: germanene, and Sn: stanene) beyond graphene.[7-15] In particular, several studies on silicene have been reported since 2012, and the first silicene transistor was fabricated in 2015.[11] Following silicene, several research groups have reported the growth of germanene on Au(111)[12,13] and Al(111)[14] substrates, and stanene on a Bi_3Te_3(111) substrate.[15] Except for graphene, atomic layers of group-IV elements have tunable band gaps produced by the electric field.[16] In addition, they have larger spin-orbit coupling strengths, which may lead to a detectable quantum spin Hall effect (QSHE) and other attractive properties.[17-19] Nonetheless, the development of much more facile and practical processing methods has remained a challenging issue. The most difficult problem is that silicene grows on specific substrates and is stable only under vacuum conditions.[9,10,20,21] Another issue is that the influence of the substrate cannot be removed, probably strong hybridization between Si and the substrate may stabilize silicene grown on specific substrates.[9,20-22]

In a previous report on calcium-intercalated silicene ($CaSi_2$), we observed a massless Dirac-cone band dispersion at the k-point in the Brillouin zone, which was located far from the Fermi level because of the substantial charge transfer from the Ca atoms to the silicene layers.[23] This result is similar to the previously reported band structures of silicenes deposited on specific substrates[10] because $CaSi_2$ is a type of Zintl silicide, in which the formal charge is rewritten as Ca^{2+} and Si^{-}.[24] Therefore, the intrinsic electronic structure of silicene has never been observed. In the calculated results, a van der Waals bonded silicene layer was deposited on an intact multi-CaF_2 layer.[25] If the Ca layer of $CaSi_2$ had been exchanged with a CaF_2 layer, then the influence of the substrate would have been almost completely suppressed. To reduce the influence of external factors on the electronic structure of silicene (for example, from substrates or counter ions) and to increase the stability under ambient conditions, we replaced monolayer silicene with bilayer silicene.

The existence of a bilayer silicene structure, of which the density of unsaturated silicon bonds is reduced with

respect to that of monolayer silicene, has been predicted by molecular dynamics (MD) calculations.[26-33] If a similar bilayer silicene could be experimentally prepared, then its intrinsic electronic structure could be investigated. The electron transfer from calcium cations means the monolayer silicene in $CaSi_2$ is a formally anionic layer;[23] however, when the calcium cations become electrically neutral, the silicene will not retain its honeycomb structure and will reconstruct to form a more stable structure. Under this supposition, we have attempted to segregate the Ca and Si phases while maintaining the layer structures by the diffusion of fluoride (F) atoms, which are more electronegative than Si, into $CaSi_2$; the goal was to form an ionic bond (or interaction) between Ca and F. In this study, a BF_4 anion based ionic liquid was used to provide fluoride anions.

We have recently realized two types of bilayer silicenes (stacking two honeycomb layers with mirror or inversion symmetry), and identified new 2D crystals of bilayer silicene in the fluorinated crystallites of $CaSi_2$.[1] Furthermore, the same types of bilayer germanenes have also been synthesized in fluorinated $CaGe_2$ crystallites.[2] The new 2D crystal structure has an atomic arrangement that consists of 4-, 5-, and 6-membered rings of Si or Ge atoms (as shown in **Fig. 1**) that form a wavy shape, which are denoted as w-BLSi and w-BLGe, respectively. It should be noted that fluorination in the $CaSi_2$ and $CaGe_2$ crystallites does not proceed homogeneously. The $CaSi_2$ single crystallite was changed to a $CaSi_2F_X$ ($0 \leqq x \leqq 2.3$) compound through the diffusion of F anions (F^-) by annealing in 1-butyl-3-methylimidazolium tetrafluoroborate ([BMIM][BF_4]) ionic liquid at 250-300°C, in which the local F^- concentration gradually decreased from the crystal edge to the interior (**Figs. 2**(a) and (b)). Figure 2(c) shows a high-angle annular dark field scanning transmission electron microscopy (HAADF-STEM) image of the $CaSi_2F_{1.8}$ compound, where alternate stacking of planar crystal domains with layer thicknesses of 1-2 nm is observed. HAADF-STEM imaging provided an atomic-scale Z-contrast image (Z: atomic number) to distinguish the heavier constituent elements.[34-36]

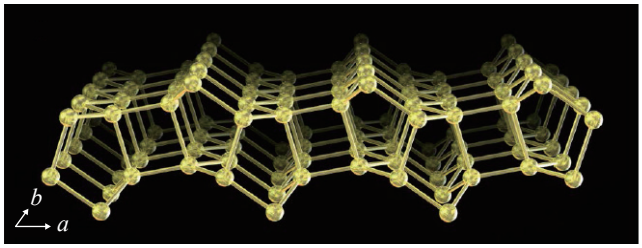

Fig. 1 Schematic illustration of the w-BLSi atomic structure.

After annealing in the [BMIM][BF_4] ionic liquid, the $CaGe_2$ crystallite was also converted into a $CaGe_2F_X$ ($0 \leq X \leq 1.8$) compound by the diffusion of F^- ions, similar to the formation of $CaSi_2F_X$ (**Figs. 3**(a) and (b)). Figure 3(c) shows HAADF-STEM images for each $CaGe_2F_X$ (X = 0.2, 0.8 and 1.5) compound. Figure 3(c)-iii shows alternate stacking of planar crystal domains with layer thicknesses of 1–2 nm, as with $CaSi_2F_X$. These bright and dark contrast domains were identified as Ge and CaF_2 phases, respectively, by STEM-energy dispersive X-ray spectroscopy (EDX) elemental mapping (Fig. S3 in Ref. (2)). The transformation from $CaGe_2$ to the Ge and CaF_2 phases with preservation of the layer structure thus occurred in $CaGe_2F_{0.8}$, as was the case with the $CaGe_2F_X$ compounds. Several types of planar crystals were identified in the $CaGe_2F_X$ ($0.2 \leq X \leq 1.0$) compounds: three types of bilayer germanenes, three types of trilayer germanenes, and bilayer and trilayer CaF_2. The majority of the types in the $CaGe_2F_X$ compounds is dependent on the F concentration (Fig. 3(d) in Ref. (2)). **Figure 4** show enlarged HAADF-STEM images taken from the regions including the w-BLSi or w-BLGe planar crystals in the $CaSi_2F_{1.8}$ and the $CaGe_2F_{0.8\text{-}1.0}$ compounds. In those images, novel planar crystals of w-BLSi and w-BLGe have commensurate structures with Si, Ge and CaF_2 crystals. In practice, it is a most challenging task to solve the structures of new 2D crystals in thin layered multiphase composites.

To determine an unknown crystal structure, the single crystal X-ray diffraction (XRD) method is generally the most powerful technique when the unknown crystal is obtained as a single phase with sufficiently large dimensions and no crystal defects. However, most novel crystallites have crystal defects, domain structures, and multiple phases. In such a case, it is impossible to solve the unknown crystal structure by the XRD method only. Electron crystallography (EC), which is a method to derive the crystal structure using electron diffraction patterns and atomic resolution transmission electron microscopy (TEM) and/or STEM images, is an alternative way to determine atomic configuration

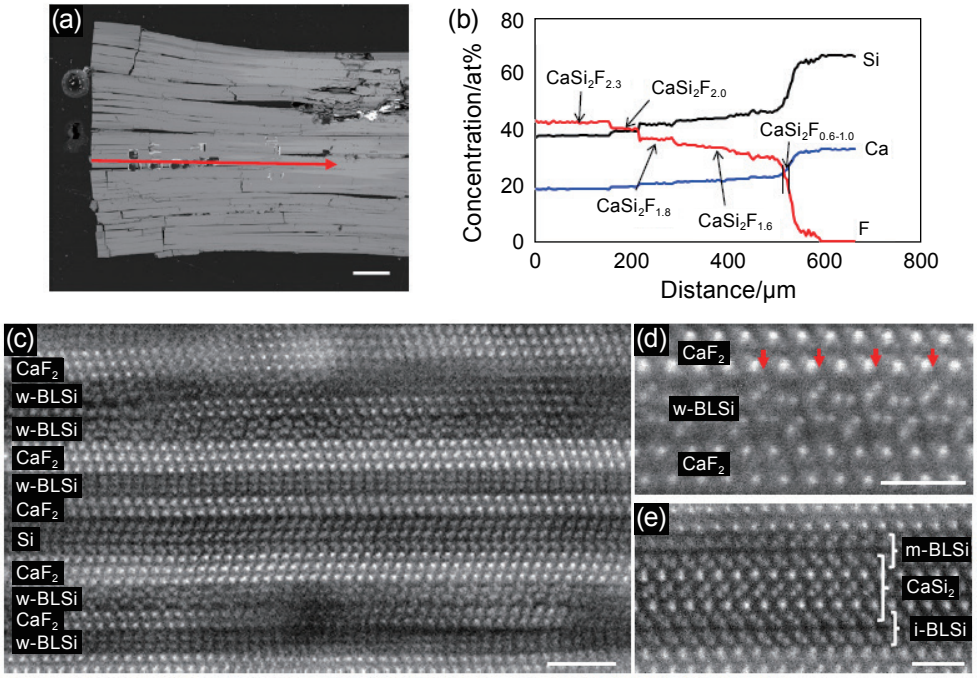

Fig. 2 (a) Cross-sectional BSE image of the crystal grain including the $CaSi_2F_X$ compound. (b) EPMA quantitative line analysis results along the red arrow in (a). (c) HAADF-STEM image from the region with $CaSi_2F_{1.8}$ in (b); the strip contrast corresponds to Si (dark domain) and CaF_2 (bright domain) planar crystals. (d) Enlarged HAADF-STEM image from the region with $CaSi_2F_2$ in (b); red arrows indicate an F-vacancy site. (e) HAADF-STEM image from the region with $CaSi_2F_{0.6\text{-}1.0}$ in (b); bright spot contrast that corresponds to the projected atomic positions of m-and i-BLSi can be observed in the image.

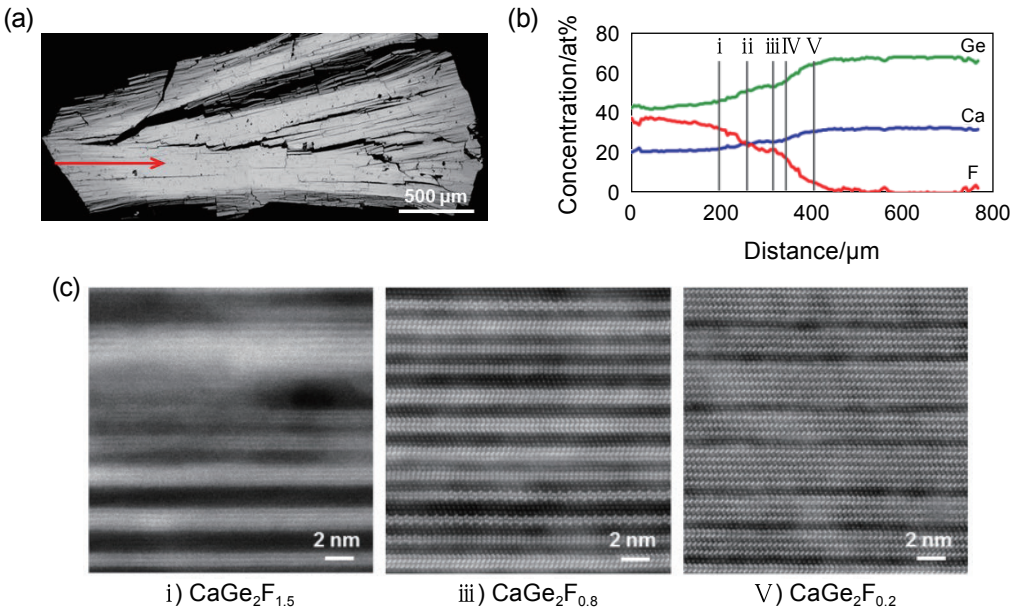

Fig. 3 (a) Cross sectional BSE image of the crystal grain of $CaGe_2F_X$, (b) EPMA quantitative line analysis results along the red arrow in the crystal grain of (a), and (c) HAADF-STEM images taken from each $CaGe_2F_X$ (X = 0.2, 0.8 and 1.5) composition in (b).

in an unknown crystal that exists as one of the multiple phases in crystallites and/or including many crystal defects. Since the 1990s, some crystal structures of newly synthesized compounds have been revealed using EC.[37-44] For example, in 1994, a framework structure consisting of Ti, Si and O atoms in the microporous titanosilicate ETS-10 were first revealed by the trial and error method using EC together with short range order information obtained using nuclear magnetic resonance spectroscopy (NMR). Despite the expectation of using ETS-10 as a catalyst from its first synthesis in 1989, the crystal structure could not be solved because of so many stacking faults included in the synthesized crystallites. From the EC results, the characteristic features in the framework structure of 12- and 7-membered rings of -Ti-O-Si- and 1D chain of -Ti-O- were revealed.[37] Furthermore, from the early 2000s, a method of automated diffraction tomography (ADT) combined with precession electron diffraction (PED) was developed, and ab initio determinations of some 3D crystal structures were demonstrated.[45] ADT-PED seems to be a most powerful and sophisticated technique for the determination of small crystallites with sizes of several tens nanometers. However, in the case for w-BLSi, it is too difficult to apply ADT-PED for 2D planar crystals or multiphase crystallites with domain thicknesses of a few nanometers. Therefore, to determine the 2D structure of bilayer silicene, we had to use the trial and error method (similar to the case of ETS-10) using HAADF-STEM and high resolution TEM (HRTEM) images with the following procedure:

(1) Determine chemical composition by EDX elemental analysis;
(2) Measure lattice parameters from HRTEM images;
(3) Construct an atomic model from projected atom positions and interfacial symmetries of the neighboring crystallites of CaF_2 obtained from HAADF-STEM images through trial and error approach together with deep insights;
(4) Measure projected atom positions as accurately as possible;
(5) Refine the atom positions of the derived structure by MD calculation;

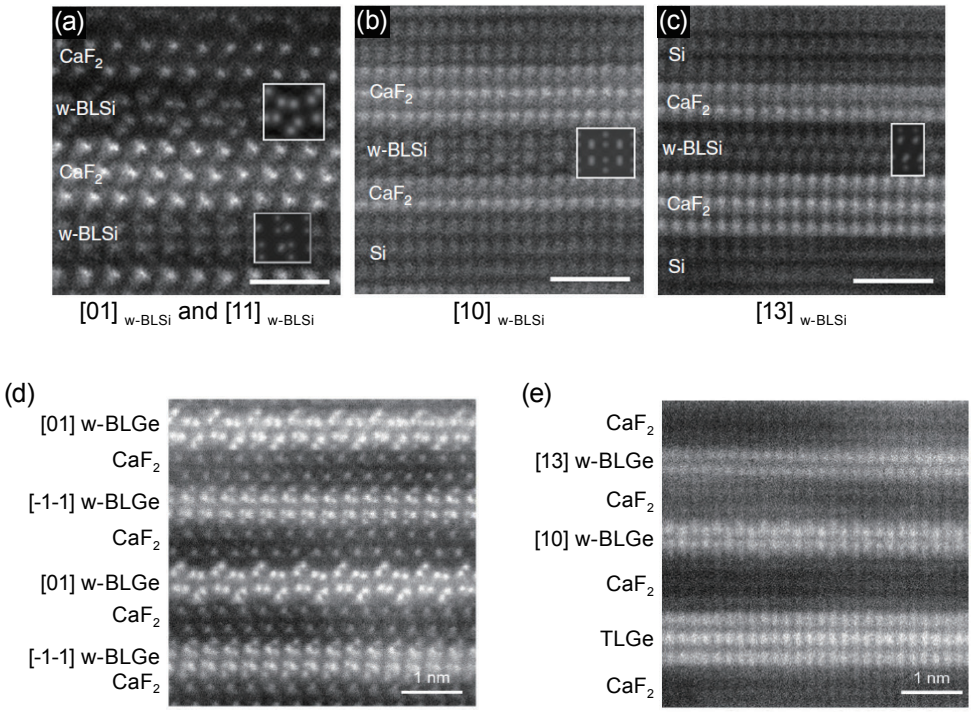

Fig. 4 HAADF-STEM images of (a)-(c) w-BLSi and (d), (e) w-BLGe taken with the incident beam along (a) the $[01]_{w\text{-}BLSi}$ and $[11]_{w\text{-}BLSi}$ (// $[1\text{-}10]_{CaF_2}$) directions, (b) the $[10]_{w\text{-}BLSi}$ (// $[11\text{-}2]_{Si\ and\ CaF_2}$) direction, (c) the $[13]_{w\text{-}BLSi}$ (// $[11\text{-}2]_{Si\ and\ CaF_2}$) direction, (d) the $[01]_{w\text{-}BLGe}$ and $[\text{-}1\text{-}1]_{w\text{-}BLGe}$ (// $[1\text{-}10]_{CaF_2}$) directions, and (e) the $[13]_{w\text{-}BLGe}$ and $[10]_{w\text{-}BLGe}$ (// $[11\text{-}2]_{CaF_2}$) directions.

(6) Compare observed HAADF-STEM images and simulated images using the derived structure.

In the present work, we review the procedure for determination of the 2D crystal structure of w-BLSi, followed by a discussion on F vacancies at the interfacial plane between w-BLSi and CaF_2 layers.

2. Procedure for Determination of the 2D Crystal Structure

Details for the synthesis of $CaSi_2F_X$ and $CaGe_2F_X$ are described in Refs. (1) and (2). Atomic resolution STEM (FEI, Titan^3 G2) equipped with an aberration corrector for scanning electron probe and wide detection area EDX detectors were used. Such highest performance facilities are required to determine the unknown 2D crystal structure. The commercial MacTempasX^{TM} (Total Resolution) software package was used for HAADF-STEM image simulations.

2. 1 Chemical Composition of w-BLSi

Figure 5 shows an HAADF-STEM image and STEM-EDX elemental maps for Ca, F and Si. The Si layers are clearly segregated from layers that consist of Ca and F. Si layers with thicknesses of 1–2 nm and Ca-F layers of similar thickness are alternately stacked. The results suggest the new 2D crystal (w-BLSi) is made from Si.

2. 2 2D Lattice Parameters of w-BLSi

HAADF-STEM image at high magnification with atomic resolution often suffers distortion due to specimen drift during the scan time. Thus, the lattice parameters of w-BLSi were determined using HRTEM images as accurately as possible. HAADF-STEM and HRTEM images of the CaF_2 region were used as standard images to calibrate the magnification and distortion. **Figures 6**(a) and (b) show HRTEM images taken with the incident direction parallel to the $[1\text{-}10]_{CaF_2}$ and the $[11\text{-}2]_{CaF_2}$ directions. The 2D translation periods of w-BLSi were determined from the flat regions of w-BLSi (red arrows) in Figs. 6(a) and (b) to be a = 0.661(2) nm and b = 0.382(3) nm, and the two translation axes were normal to each other, following the calibrated magnification of an HRTEM image of the $CaSi_2$ raw material, with an estimated error of less than 1%. The a period of w-BLSi is similar to the triple lattice spacing of $d_{11\text{-}2}$ in CaF_2 (0.223 nm), and the b period is similar to $d_{\text{-}110}$ in CaF_2 (0.386 nm), i.e., the difference between w-BLSi and CaF_2(111) is less than the observation error.

The atomic arrangement of the CaF_2(111) plane

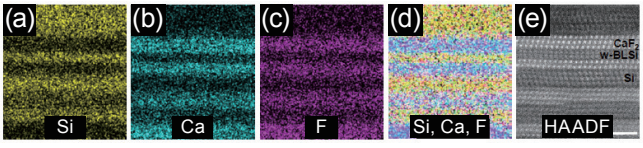

Fig. 5 STEM-EDX elemental mapping results of the $CaSi_2F_2$ composition region. One-element maps of (a) Si, (b) Ca, (c) F, and (d) overlapped-map of each, and (e) HAADF-STEM image of the mapping area. The scale bar in (e) is 1 nm.

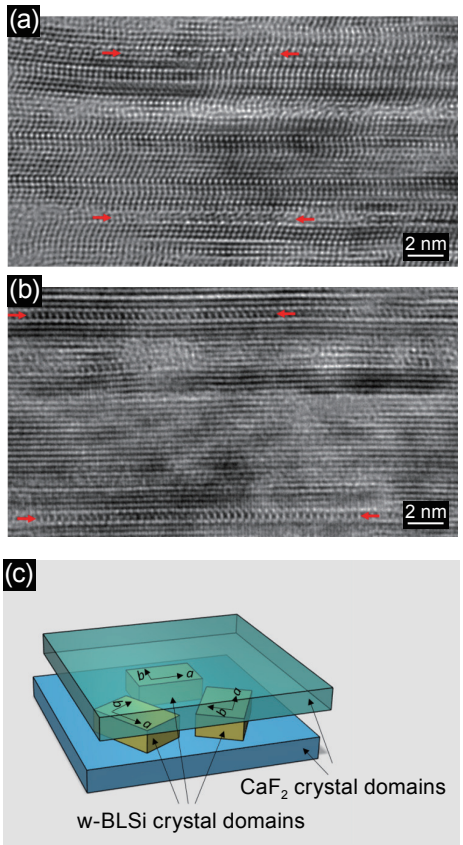

Fig. 6 HRTEM images taken along (a) the $[01]_{w\text{-}BLSi}$ ($[1\text{-}10]_{Si\ and\ CaF_2}$) and (b) $[10]_{w\text{-}BLSi}$ ($[11\text{-}2]_{Si\ and\ CaF_2}$) incident directions. The red arrows indicate the w-BLSi positions. (c) Three equivalent relative rotation angles between w-BLSi and the CaF_2(111) planes.

exhibited threefold symmetry; therefore, three equivalent relative rotation angles were observed between w-BLSi and the CaF_2(111) plane. The angle between the $[01]_{w\text{-}BLSi}$ and $[11]_{w\text{-}BLSi}$ directions was almost 60°. Figure 6(c) shows the orientational relationship between CaF_2 and w-BLSi.

2. 3 Atomic Model of w-BLSi

HAADF-STEM images taken with the incident directions along the [1-10] and [11-2] directions of the CaF_2 crystal show complex contrast at the w-BLSi regions neighboring the CaF_2 layers (Fig. 4). The w-BLSi layer is always sandwiched between CaF_2 thin-layered crystals (with thicknesses of 2 or 3 layers). Figure 4(a) shows two different arrangements of bright dot contrasts in the w-BLSi regions, which correspond to the projection of atom columns of the crystal along the incident direction of electron beam. HAADF-STEM images of CaF_2 taken with the [11-2] incident direction also show two different arrangements of bright dot contrasts in the w-BLSi regions (Figs. 4(b) and (c)). Four types of atom column arrangements can be recognized in the w-BLSi regions. Assuming that the four types of atom column arrangements correspond to projections along the four different directions of the same crystal consisting of Si atoms only, we constructed a unique model of a Si atom network (framework structure), as shown in **Fig. 7**(a), by trial and error using small plastic model parts. Although we considered several frameworks, the model shown in Fig. 7(a) is the only one that corresponds to the atom column arrangements of the HAADF-STEM images. Figure 7(b) shows schematic drawings of the projected framework structure along several directions. The framework model is a rectangular 2D crystal with a 2D space group of *pm*, and lattice parameters *a* close to the triple lattice spacing of d_{112} of CaF_2 and *b* close to d_{110} of CaF_2. According to the 2D lattice of the framework model, the four directions in Fig. 4 can be assigned as [10], [11], [13] and [01], respectively. It should be noted that the angle between the [10] and [13] directions is almost 60° and that the angle between [01] and [11] is also 60°.

2. 4 Projected Atom Positions

To compare the contrast of the observed and simulated images, the atom positions in the model structure should be as accurate as possible. The projected atom positions of w-BLSi along the incident direction of electron beam were measured from the bright dot contrast in the HAADF-STEM images with correction of the image distortions by reference to the atom column positions in the nearest neighbor CaF_2 crystal regions (**Fig. 8**(a)). The measurement of peak positions was aided by in-house built software to refine the positions by the non-linear least squares method, as assuming a 2D Gaussian intensity distribution (Fig. 8(b)). More than 100 peak positions were measured, and averaged values for each eight atom positions in the unit cell were obtained (**Table 1**).

2. 5 Refinement of Atom Positions for the Derived Structure by Ab Initio MD Calculation

The procedure to determine new structures frequently applies refinement of the atom positions by MD calculations to obtain the minimum-energy structure. Average atomic positions of the w-BLSi structure were determined from the ab initio MD results, as

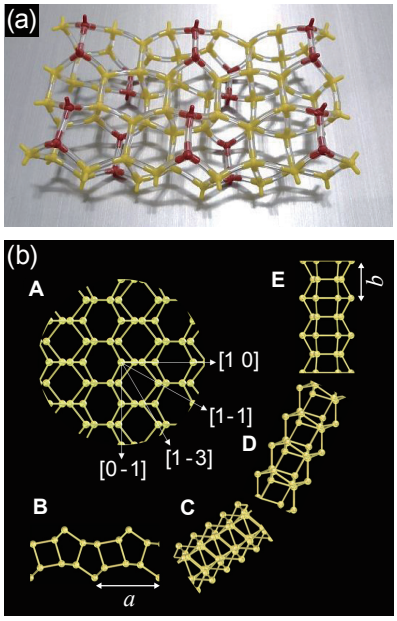

Fig. 7 (a) Photograph of a structural model of w-BLSi made from plastic model parts (yellow and red) with flexible tubes (transparent). (b) Schematic drawings of the projected structures of w-BLSi in each direction. A. Stacking direction. B. [01] direction. C. [13] direction. D. [11] direction. E. [10] direction.

shown in **Table 2**, which is the structure obtained in the quenching process at 0 K in the ab initio MD simulation.[1] The experimentally determined lattice parameters a and b were employed in the ab initio MD run. The atom positions in the BLSi structure calculated by MD show good agreement with those of the experimentally observed w-BLSi structure in Table 1.

The refined w-BLSi framework structure seems to have some symmetry elements, including a mirror plane perpendicular to the b-axis, an inversion center at the center of the four-membered ring, and a twofold axis running through the center of the four-membered ring parallel to the b-axis. Therefore, we could define a monoclinic 3D unit cell with a = 0.661 nm, b = 0.382 nm, c = 0.710 nm, and β = 67° and the space group $P2/m$ (No. 10), as shown in **Fig. 9**. **Table 3** shows the lattice constants, space group and atomic

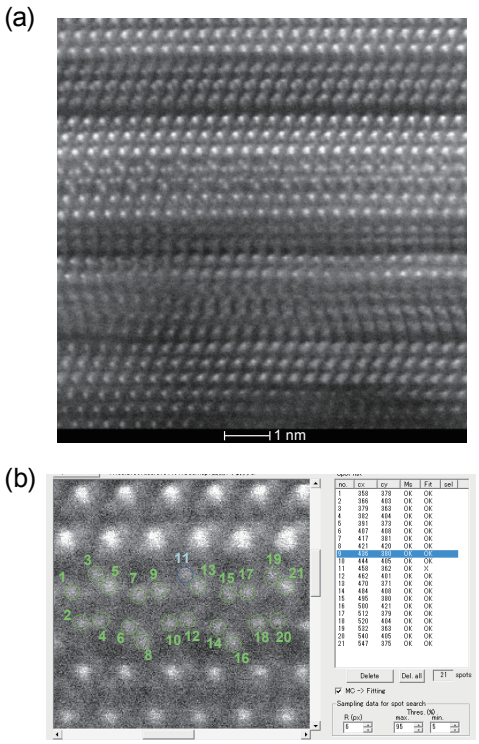

Fig. 8 (a) HAADF-STEM image taken from the region with the $CaSi_2F_2$ composition. (b) A part of window of the in-house built software for measurements of peak positions.

Table 1 Crystal structure parameters for the w-BLSi crystal regarded as a 3D crystal.

Lattice parameter: a = 0.661(2) nm, b = 0.382(3) nm, c = 0.653(9) nm, $\alpha = \beta = \gamma = 90°$				
No.	x	y	z	Occ.
1	0.11(2)	0	0.67(1)	1
2	0.34(2)	0.5	0.65(1)	1
3	0.67(3)	0.5	0.71(3)	1
4	0.83(1)	0	0.88	1
5	0.00(1)	0	0.33(2)	1
6	0.29(1)	0	0.12(4)	1
7	0.46(2)	0.5	0.31(3)	1
8	0.79(2)	0.5	0.35(1)	1

Table 2 Crystal structure parameters for the w-BLSi crystal from the MD calculated result.

Lattice parameter: a = 0.661 nm, b = 0.382 nm, c = 0.655 nm, $\alpha = \beta = \gamma = 90°$				
No.	x	y	z	Occ.
1	0.140(4)	0.999(3)	0.674(2)	1
2	0.344(2)	0.499(3)	0.637(5)	1
3	0.698(3)	0.501(5)	0.717(3)	1
4	0.837(5)	0.001(5)	0.881(3)	1
5	0.000(4)	0.999(4)	0.334(3)	1
6	0.293(3)	0.002(4)	0.115(4)	1
7	0.436(2)	0.502(4)	0.279(4)	1
8	0.794(3)	0.501(5)	0.362(2)	1

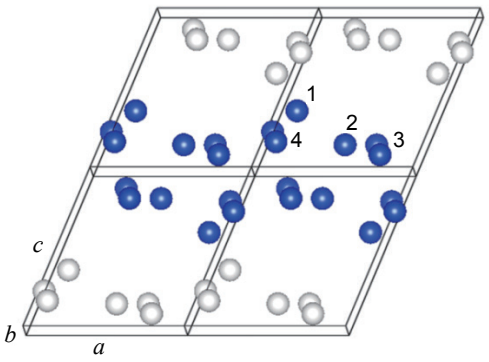

Fig. 9 Schematic drawing of the monoclinic 3D unit cell of the w-BLSi crystal obtained from the ab initio MD result.

Table 3 Crystal structure parameters for the w-BLSi crystal from the MD calculation result regarded as a monoclinic 3D unit cell.

Lattice parameter: a = 0.661 nm, b = 0.382 nm, c = 0.710 nm, β = 67°, space group $P2/m$ (10)						
No.	Wyckoff pos.	Sym.	x	y	z	Occ.
1	2 n	m	0.113(3)	0.5	0.382(3)	1
2	2 n	m	0.500(3)	0.5	0.169(2)	1
3	2 m	m	0.719(2)	0	0.137(3)	1
4	2 m	m	0.040(2)	0	0.219(3)	1

positions of the 3D w-BLSi crystal derived from the ab initio MD result.

2. 6 HAADF-STEM Image Simulation

HAADF-STEM image simulations were performed using the structural parameters from the ab initio MD result in Table 2. The simulated images of w-BLSi with the incident directions along the [01], [11], [10] and [13] directions are shown as insets in Figs. 4(a)-(c), respectively. The contrasts in the simulated images show good agreement with those of the observed images.

To confirm that the image contrast corresponds to the atomic arrangement including the interface of two or more different phases or orientations, some interface models with different configurations were constructed. Long-period stacking structure models (**Fig. 10**(b)) with the same stacking sequence as in Fig. 10(a) were used to perform HAADF-STEM image simulations, then the relative position between w-BLSi and the CaF_2 crystals as well as the F site occupancy on the CaF_2(111) surface are confirmed. As shown in Fig. 10(c), the simulated image calculated by the model with vacancies in half of the F sites shows better agreement with the observed contrast than that without vacancies (Fig. 10(d)). In addition, Figs. 10(e)-(g) show HAADF-STEM simulation images of the long-period stacking structure model of the $[11]_{w\text{-}BLSi}$, $[10]_{w\text{-}BLSi}$ and $[13]_{w\text{-}BLSi}$ incident directions. In each image, contrasts of Si, CaF_2, and w-BLSi agree well with those in the observed images (Figs. 4(a)-(c)).

Once the w-BLSi structure had been solved, the structure of the w-BLGe present in fluorinated $CaGe_2$ could be determined easily because the contrast of the HAADF-STEM images of w-BLGe show remarkably

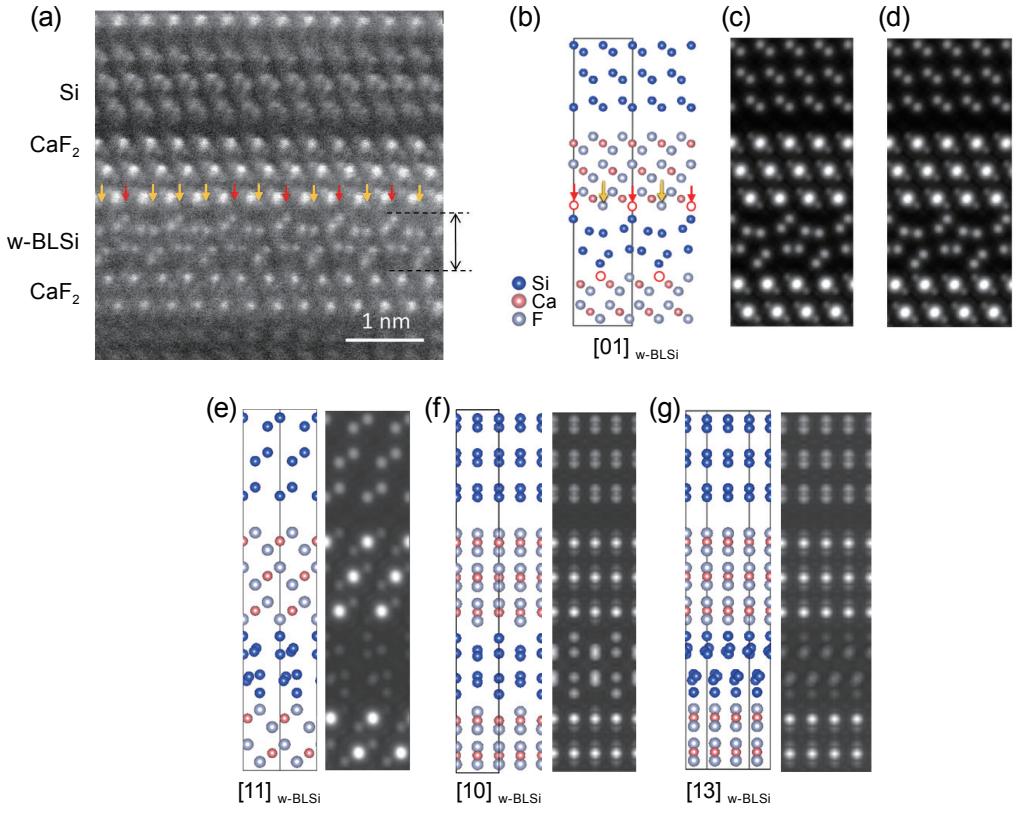

Fig. 10 (a) $[-110]_{Si\ and\ CaF_2}$ and $[01]_{w\text{-}BLSi}$ incident direction HAADF-STEM image of Si, CaF_2 and the w-BLSi formed area. F atoms (yellow arrows) and vacancies (red arrows) almost alternately substitute for F sites at the interface between w-BLSi and CaF_2. (b) The long-period stacking structure model, which consists of bilayer CaF_2, w-BLSi, trilayer CaF_2 and Si, based on the HAADF-STEM image of (a). F atoms (yellow arrows) and vacancies (red arrows) alternately substitute for F sites at the interface between w-BLSi and CaF_2. Simulated images calculated by MacTempasX using structure models (c) with and (d) without vacancies in the F site. Projected model and simulated image of (b) along (e) the $[11]_{w\text{-}BLSi}$ direction, (f) the $[10]_{w\text{-}BLSi}$ direction, and (g) the $[13]_{w\text{-}BLSi}$ direction. HAADF-STEM image simulations were conducted under the condition of a 3.8 nm specimen thickness.

similar features to those of w-BLSi. The differences of the two structures are lattice parameters and bond length. In particular, the lattice constant of *c* for w-BLGe, which corresponds to the thickness of the bi-layer, is clearly different from that of w-BLSi (Table S1 in Ref. (2)).

3. Discussion of Faint Contrasts to Determine F Vacancies

In almost all of the observed HAADF-STEM images, w-BLSi always faced the (111) plane of CaF_2, and the F^- vacancies (red arrows in Fig. 2(d)) on the CaF_2(111) surface were recognised at special positions associated with the wavy structure of w-BLSi. As shown in Fig. 10, F^- vacancies seem to be detectable in the HAADF-STEM image contrast. We attempted to clarify the quantity of F^- vacancies. HAADF-STEM image simulations were performed to confirm the occupancy of F atoms at the vacancy sites (red arrows in Fig. 2(d)). **Figure 11** shows observed and simulated HAADF-STEM images for occupancies ranging from 0.0 to 1.0. Line profiles obtained from the observed and simulated images are shown in Figs. 11(c) and (d). The former was obtained from an average of the line profiles with or without a vacancy, whereas the latter was the simulation result obtained by varying the occupancy from 0.0 to 1.0. The occupancy of F atoms at the vacancy sites can be estimated to be less than 0.4 by comparison of the observed and simulated profiles (black arrows in Fig. 11).

4. Conclusions

Although it is fortunate that the new 2D crystal structure of w-BLSi has higher symmetries and easily comprehensible correlation with neighboring layers of CaF_2, we have spent a half year from the first HAADF-STEM image observation until a successful solution of the new 2D structure. Even if TEM performance and structural determination techniques are enhanced in the future, to solve unknown crystal structures still requires concentration of our own deep insights, wide knowledge and persistence to apply the trial and error method, as shown in the present review. We strongly expect that new structures will be solved by using the material informatics techniques (or something else) and that the accuracy of structural refinement will continue to improve.

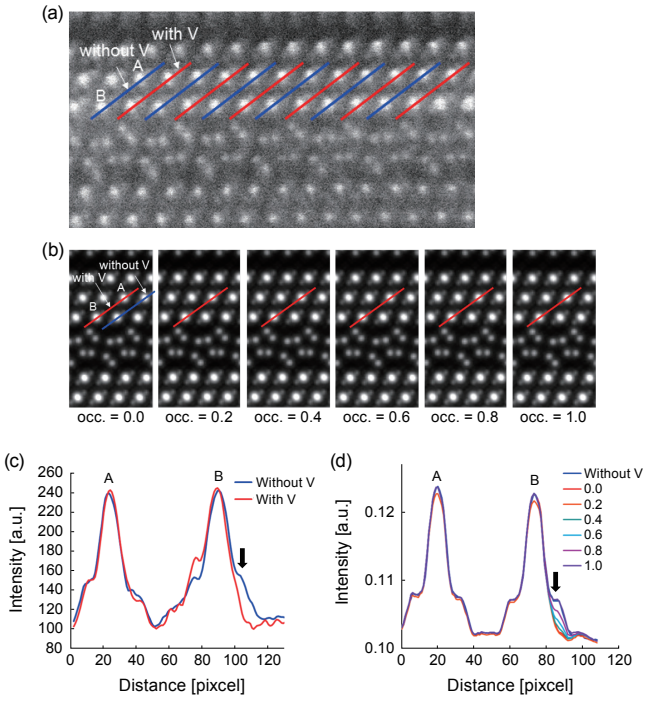

Fig. 11 (a) An observed HAADF-STEM image. (b) Simulated HAADF-STEM images foroccupancies of F atoms ranging from 0.0 to 1.0. Line profile positions with a vacancy and without a vacancy are indicated by red and blue lines, respectively. (c) Average of line profiles with or without a vacancy in the observed HAADF-STEM image of (a). (d) Line profiles of simulated images of (b).

Acknowledgements

This work was supported in part by PRESTO, the Japan Science and Technology Agency, and by a Grant-in-Aid for Scientific Research from the Ministry of Education, Culture, Sports, Science and Technology (MEXT), Japan. HAADF-STEM observations in this work were supported by the "Nanotechnology Platform" of MEXT, Japan, at the Center for Integrated Nanotechnology Support, Tohoku University. Computations were undertaken with the assistance of resources from the National Computational Infrastructure (NCI), which is supported by the Australian Government, the Pawsey Supercomputing Centre with funding from the Australian Government and the Government of Western Australia, the Multi-modal Australian ScienceS Imaging and Visualisation Environment (MASSIVE), and the Victorian Partnership for

Advanced Computing Limited (VPAC Ltd) through the V3 Alliance, Australia, and at the computational facilities at the Research Center for Computational Science, National Institute of Natural Sciences, and at the Research Institute for Information Technology, Kyushu University, Japan. The authors thank Dr. T. Morishita for MD calculations, Mr. Y. Hayasaka for the HAADF-STEM observations and EDX analyses, Mr. Y. Yagi for the EPMA measurements, and Prof. S. Yamanaka and Dr. Y. Takeda for fruitful discussion.

References

(1) Yaokawa, R. et al., "Monolayer-to-bilayer Transformation of Silicenes and Their Structural Analysis", *Nature Commun.*, Vol. 7 (2016), 10657.
(2) Yaokawa, R. et al., "Multilayer Germanenes Formed in Zintl-phase $CaGe_2$ by Fluoride Diffusion", *ChemistrySelect*, Vol. 1, No. 17 (2016), pp. 5579-5583.
(3) Novoselov, K. S. et al., "Two-dimensional Gas of Massless Dirac Fermions in Graphene", *Nature*, Vol. 438 (2005), pp. 197-200.
(4) Zhang, Y. et al., "Experimental Observation of the Quantum Hall Effect and Berry's Phase in Graphene", *Nature*, Vol. 438 (2005), pp. 201-204.
(5) Britnell, L. et al., "Strong Light-matter Interactions in Heterostructures of Atomically Thin Films", *Science*, Vol. 340, No. 6138 (2013), pp. 1311-1314.
(6) Mak, K. F. et al., "The Valley Hall Effect in MoS_2 Transistors", *Science*, Vol. 344, No. 6191 (2014), pp. 1489-1492.
(7) Takeda, K. and Shiraishi, K., "Theoretical Possibility of Stage Corrugation in Si and Ge Analogs of Graphite", *Phys. Rev. B*, Vol. 50, No. 20 (1994), pp. 14916-14922.
(8) Cahangirov, S. et al., "Two- and One-dimensional Honeycomb Structures of Silicon and Germanium", *Phys. Rev. Lett.*, Vol. 102, No. 23 (2009), 236804.
(9) Vogt, P. et al., "Silicene: Compelling Experimental Evidence for Graphenelike Two-dimensional Silicon", *Phys. Rev. Lett.*, Vol. 108, No. 15 (2012), 155501.
(10) Fleurence, A. et al., "Experimental Evidence for Epitaxial Silicene on Diboride Thin Films", *Phys. Rev. Lett.*, Vol. 108, No. 24 (2012), 245501.
(11) Tao, L. et al., "Silicene Field-effect Transistors Operating at Room Temperature", *Nat. Nanotechnol.*, Vol. 10 (2015), pp. 227-231.
(12) Dávila, M. E. et al., "Germanene: A Novel Two-dimensional Germanium Allotrope Akin to Graphene and Silicone", *New J. Phys.*, Vol. 16 (2014), 095002.
(13) Dávila, M. E. and Lay, G. L., "Few Layer Epitaxial Germanene: A Novel Two-dimensional Dirac Material", *Sci. Rep.*, Vol. 6 (2016), 20714.
(14) Derivaz, M. et al., "Continuous Germanene Layer on Al(111)", *Nano Lett.*, Vol. 15, No. 4 (2015), pp. 2510-2516.
(15) Zhu, F.-F. et al., "Epitaxial Growth of Two-dimensional Stanine", *Nat. Mater.*, Vol. 14 (2015), pp. 1020-1025.
(16) Ni, Z. et al., "Tunable Bandgap in Silicene and Germanene", *Nano Lett.*, Vol. 12, No. 1 (2012), pp. 113-118.
(17) Liu, C.-C., Feng, W. and Yao, Y., "Quantum Spin Hall Effect in Silicene and Two-dimensional Germanium", *Phys. Rev. Lett.*, Vol. 107, No. 7 (2011), 076802.
(18) Ezawa, M., "Monolayer Topological Insulators: Silicene, Germanene, and Stanene", *J. Phys. Soc. Jpn.*, Vol. 84, No. 12 (2015), 121003.
(19) Acun, A. et al., "Germanene: The Germanium Analogue of Graphene", *J. Phys.: Condens. Matter*, Vol. 27, No. 44 (2015), 443002.
(20) Morishita, T. et al., "A New Surface and Structure for Silicene: Polygonal Silicene Formation on the Al(111) Surface", *J. Phys. Chem. C*, Vol. 117, No. 42 (2013), pp. 22142-22148.
(21) Gao, J. and Zhao, J., "Initial Geometries, Interaction Mechanism and High Stability of Silicene on Ag(111) Surface", *Sci. Rep.*, Vol. 2 (2012), Article No. 861.
(22) Cahangirov, S. et al. "Electronic Structure of Silicene on Ag(111): Strong Hybridization Effects", *Phys. Rev. B*, Vol. 88, No. 3 (2013), 035432.
(23) Noguchi, E. et al., "Direct Observation of Dirac Cone in Multilayer Silicene Intercalation Compound $CaSi_2$", *Adv. Mater.*, Vol. 27, No. 5 (2015), pp. 856-860.
(24) Yaokawa, R., Nakano, H. and Ohashi, M., "Growth of $CaSi_2$ Single-phase Polycrystalline Ingots Using the Phase Relationship between $CaSi_2$ and Associated Phases", *Acta Mater.*, Vol. 81 (2014), pp. 41-49.
(25) Kokott, S. et al., "Nonmetallic Substrates for Growth of Silicene: An Ab Initio Prediction", *J. Phys.: Condens. Matter*, Vol. 26, No. 18 (2014), 185002.
(26) Morishita, T. et al., "Surface Reconstruction of Ultrathin Silicon Nanosheets", *Chem. Phys. Lett.*, Vol. 506, No. 4-6 (2011), pp. 221-225.
(27) Sakai, Y. and Oshiyama, A., "Structural Stability and Energy-gap Modulation through Atomic Protrusion in Freestanding Bilayer Silicone", *Phys. Rev. B*, Vol. 91, No. 20 (2015), 201405(R).
(28) Morishita, T., Nishio, K. and Mikami, M., "Formation of Single- and Double-layer Silicon in Slit Pores", *Phys. Rev. B*, Vol. 77, No. 8 (2008), 081401(R).
(29) Bai, J., Tanaka, H. and Zeng, X. C., "Graphene-like Bilayer Hexagonal Silicon Polymorph", *Nano Res.*, Vol. 3, No. 10 (2010), pp. 694-700.

(30) Johnston, J. C., Phippen, S. and Molinero, V., "A Single-component Silicon Quasicrystal", *J. Phys. Chem. Lett.*, Vol. 2, No. 5 (2011), pp. 384-388.
(31) Pflugradt, P., Matthes, L. and Bechstedt, F., "Unexpected Symmetry and AA Stacking of Bilayer Silicene on Ag(111)", *Phys. Rev. B*, Vol. 89, No. 20 (2014), 205428.
(32) Guo, Z.-X. and Oshiyama, A., "Structural Tristability and Deep Dirac States in Bilayer Silicene on Ag(111) Surfaces", *Phys. Rev. B*, Vol. 89, No. 15 (2014), 155418.
(33) Cahangirov, S. et al. "Atomic Structure of the $\sqrt{3} \times \sqrt{3}$ Phase of Silicene on Ag(111)", *Phys. Rev. B*, Vol. 90, No. 3 (2014), 035448.
(34) Pennycook, S. J. and Jesson, D. E., "High-resolution Incoherent Imaging of Crystals", *Phys. Rev. Lett.*, Vol. 64, No. 8 (1990), pp. 938-941.
(35) Pennycook, S. J. and Jesson, D. E., "High-resolution Z-contrast Imaging of Crystals", *Ultramicroscopy*, Vol. 37, No. 1-4 (1991), pp. 14-38.
(36) Pennycook, S. J. and Jesson, D. E., "Atomic Resolution Z-contrast Imaging of Interfaces", *Acta Metall. Mater.*, Vol. 40 (1992), pp. S149-S159.
(37) Anderson, M. W. et al., "Structure of the Microporous Titanosilicate ETS-10", *Nature*, Vol. 367 (1994), pp. 347-351.
(38) Ohsuna, T. et al., "Framework Determination of a Polytype of Zeolite Beta by Using Electron Crystallography", *J. Phys. Chem. B*, Vol. 106, No. 22 (2002), pp. 5673-5678.
(39) Lu, B. et al., "Electron Crystallographic Study of $Bi_4(Sr_{0.75}La_{0.25})_8Cu_5O_y$ Structure", *Ultramicroscopy*, Vol. 70, No. 1-2 (1997), pp. 13-22.
(40) Sinkler, W. and Marks, L. D., "Dynamical Direct Methods for Everyone", *Ultramicroscopy*, Vol. 75, No. 4 (1999), pp. 251-268.
(41) Weirich, T. E. et al., "Structures of Nanometre-size Crystals Determined from Selected-area Electron Diffraction Data", *Acta Crystallogr., Sect. A: Found. Adv.*, Vol. 56, Part 1 (2000), pp. 29-35.
(42) Wagner, P. et al., "Electron Diffraction Structure Solution of a Nanocrystalline Zeolite at Atomic Resolution", *J. Phys. Chem. B*, Vol. 103, No. 39 (1999), pp. 8245-8250.
(43) Carlsson, A. et al., "The Structure of MCM-48 Determined by Electron Crystallography", *J. Electron Microscopy*, Vol. 48, No. 6 (1999), pp. 795-798.
(44) Sakamoto, Y. et al., "Direct Imaging of the Pores and Cages of Three-dimensional Mesoporous Materials", *Nature*, Vol. 408 (2000), pp. 449-453.
(45) Mugnaioli, E., Gorelik, T. and Kolb, U., "'Ab initio' Structure Solution from Electron Diffraction Data Obtained by a Combination of Automated Diffraction Tomography and Precession Technique", *Ultramicroscopy*, Vol. 109, No. 6 (2009), pp. 758-765.

Figs. 1-2, 4(a)-(c), 5-6, 7(b), 9-11 and Tables 1-3
Reprinted from Nature Commun., Vol. 7 (2016), 10657, Yaokawa, R. et al., Monolayer-to-bilayer Transformation of Silicenes and Their Structural Analysis, © 2016 Springer Nature.

Figs. 3 and 4(d)-(e)
Reprinted from ChemistrySelect, Vol. 1, No. 17 (2016), pp. 5579-5583, Yaokawa, R. et al., Multilayer Germanenes Formed in Zintl-phase $CaGe_2$ by Fluoride Diffusion, © 2016 WILEY, with permission from John Wiley & Sons.

Tetsu Ohsuna
Research Fields:
- Electron Microscopy
- Micro-, Meso-porous Materials

Academic Degree: Dr.Eng.
Academic Societies:
- The Japanese Society of Microscopy
- Japan Zeolite Association
- The Japan Institute of Metals and Materials

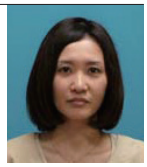

Ritsuko Yaokawa
Research Field:
- Material Science

Academic Degree: Dr.Sci.
Academic Society:
- The Japan Society of Applied Physics

Hideyuki Nakano
Research Fields:
- Low-dimensional Semi-conductive Materials
- Energy Storage Materials

Academic Degree: Dr.Eng.
Academic Societies:
- The Ceramic Society of Japan
- The Chemical Society of Japan
- The Japan Society of Applied Physics
- The Society of Silicon Chemistry JAPAN

Award:
- CerSJ Awards for Academic Achievements in Ceramic Science and Technology, The Ceramic Society of Japan, 2013

